Numerical evaluation of subsampling effects on image reconstruction in compressed sensing microscopy

Yoann Le Montagner[a,b], Elsa Angelini[b], and Jean-Christophe Olivo-Marin[a]

[a]Institut Pasteur, Unité d'Analyse d'Images Quantitative CNRS URA 2582, F-75015 Paris
[b]Institut Télécom, Télécom ParisTech CNRS LTCI, F-75013 Paris

ABSTRACT

When undergoing reconstruction through a compressed sensing scheme, real microscopic images are affected by various artifacts that lead to detail loss. Here, we discuss how the sampling strategy and the subsampling rate affect the compressed sensing reconstruction, and how they should be determined according to a targeted accuracy level of the reconstruction. We investigate the relevance and limits of theoretical results through several numerical reconstructions of test images. We discuss the quantitative and qualitative artifacts that affect the reconstructed signal when reducing the number of measurements in the Fourier domain. We conclude by extending our results to real microscopic images.

1. SUMMARY OF THEORETICAL BACKGROUND IN THE COMPRESSED SENSING FIELD

1.1 Recovering sparse data from incomplete measurements

The recent sampling theory of compressed sensing (CS) predicts that sparse signals and images can be reconstructed from what was previously believed to be incomplete information. CS was introduced by Candès, Romberg and Tao,[1] and Donoho.[2] It relies on the fact that many types of signals or images can be well-approximated by a sparse decomposition on a suitable basis.

Relying on some previous work by Donoho and Huo,[3] Donoho and Elad,[4] Candès, Romberg and Tao,[1] and Donoho[2] studied the following problem: given a signal of interest $x_0 \in \mathbb{C}^N$, a measurement matrix $F \in \mathbb{C}^{M \times N}$ with $M < N$, and an observation $y = Fx_0 \in \mathbb{C}^M$, assuming that the original signal x_0 is sparse (i.e. its number S of non-zero coefficients is much smaller than its size N: $S = \|x\|_{l_0} \ll N$), can this signal of interest be recovered only from the knowledge of the observation y? More precisely, under which conditions can x_0 be recovered as the solution of the following convex optimization program:

$$(P_1) \qquad \min_{x \in \mathbb{C}^N} \|x\|_{l_1} \quad \text{s.t.} \quad y = Fx \tag{1}$$

In (P_1), the l_1 norm must be understood as a surrogate for the l_0 pseudo-norm, whose minimization favors the solutions that agree with the sparsity prior we assume on the original signal x_0. However, direct solving of the l_0 scheme leads to intractable combinatorial problems, whereas relaxing it into (P_1) permits to use all the mathematical tools coming from the convex optimization field.

In the mid-2000, various results showed that recovering the original sparse signal x_0 from (P_1) will actually work for several classes of measurement matrix F. These results rely on the notion of *restricted isometry property*, which is a tool that somehow quantify how much the measurement matrix F behaves like an orthonormal matrix when applied to a sparse vector (see for example Candès, Romberg and Tao,[1] Candès and Tao,[5,6] Candès and Romberg,[7] or Candès[8] for more details).

Candès, Romberg and Tao[9] also extended their framework so that it could handle weakly sparse signals (i.e. signals that are not sparse, but that can be well approximated by sparse vectors) as well as noisy measurements ($y = Fx + b$ where b is a white Gaussian additive noise); in this case, they proposed to relax (P_1) into the following (P_2) problem:

$$(P_2) \qquad \min_{x \in \mathbb{C}^N} \|x\|_{l_1} \quad \text{s.t.} \quad \|y - Fx\|_{l_2} \leq \epsilon \tag{2}$$

where the regularization parameter ϵ is tuned according to the noise power. These more challenging hypothesis are also closer to real-world conditions.

1.2 Randomly subsampled orthonormal transforms

Candès and Romberg[7] studied the particular case of measurement matrices F designed by randomly subsampling orthonormal transforms, i.e. randomly selecting some rows in a given unitary matrix U. The authors studied in particular the special case where U is the discrete Fourier transform.

Randomly subsampled orthonormal transforms are particularly worth of interest, as they can lead to practical implementation of CS devices (see for example Duarte *et al.*,[10] Lustig *et al.*,[11] Marim *et al.*[12]). The use of such measurement matrices also enables to handle large dimension signals, such as images ($N \approx 10^6$), while keeping a reasonable reconstruction time, thanks to the fact that those orthonormal transforms are often associated with fast computation algorithms (see for example Le Montagner *et al.*[13]).

For the special case of measurement matrices built by randomly subsampling orthonormal transforms, Candès and Romberg[7] derived the following theorem from previous results related to the restricted isometry property:

THEOREM 1.1. *Given an original signal x_0 such that $\|x_0\|_{l_0} \leq S$ and a measurement matrix F built by randomly selecting M rows from a $N \times N$ unitary matrix U, assuming that:*

$$M \geq C \cdot \mu(U)^2 \cdot S \cdot N \log(N) \tag{3}$$

where C is a (small) numerical constant, and $\mu(U)$ is defined as the largest magnitude among the entries $u_{i,j}$ of the matrix U:

$$\mu(U) := \max_{i,j} |u_{i,j}| \tag{4}$$

Then, the program (P_1) instantiated with $y \leftarrow Fx_0$ recovers x_0 with an overwhelming probability.

This formulation assumes that the orthonormal matrix U is normalized such that $UU^* = \mathrm{Id}$; with this normalization, $\mu(U)$ is valued between $\frac{1}{\sqrt{N}}$ and 1. Please note that Candès and Romberg[7] used a different normalization.

When targeting some specific application, it can be more natural to interpret U as a product of two orthonormal matrices, in particular when the signal of interest is not sparse itself, but rather has a sparse representation in some transformed domain. This case occurs for instance with natural images, that are not sparse by themselves in general, but admit a sparse representation in a wavelet domain. To cope with this case, it is more convenient to recover the signal of interest from the following optimization problem rather than (P_1):

$$\min_{x \in \mathbb{C}^N} \|\Psi x\|_{l_1} \quad \text{s.t.} \quad \Phi x = y \tag{5}$$

where Ψ is the orthonormal transform mapping the signal's canonical domain to its sparse domain, and Φ is the measurement matrix, built by randomly selecting the rows from a given orthonormal transform $\tilde{\Phi}$. For example, in the case of CS imaging applications, it is quite common to choose the Fourier transform for $\tilde{\Phi}$, and a wavelet transform for Ψ since natural images are known to be sparse or almost sparse in wavelet basis.

As Ψ is orthonormal, (5) is equivalent to the problem formulated in theorem 1.1, with $F \leftarrow \Phi\Psi^*$ and $U \leftarrow \tilde{\Phi}\Psi^*$; in that case, the coefficient $\mu(U)$ can be interpreted as follows:

$$\mu(U) = \mu\left(\tilde{\Phi}^*, \Psi^*\right) = \max_{i,j} \left|\langle \tilde{\phi}_i^*, \psi_j^* \rangle\right| \tag{6}$$

where the vectors $\left(\tilde{\phi}_i^*\right)$ and $\left(\psi_j^*\right)$ represents the rows of respectively $\tilde{\Phi}$ and Ψ. In (6), $\mu\left(\tilde{\Phi}^*, \Psi^*\right)$ represents the mutual incoherence between the two orthonormal basis $\tilde{\Phi}^*$ and Ψ^*, which is a notion introduced by Donoho and Huo:[3] a small value for $\mu\left(\tilde{\Phi}^*, \Psi^*\right)$ characterizes the fact that *no nonzero signal can have a sparse representation in both basis simultaneously.*

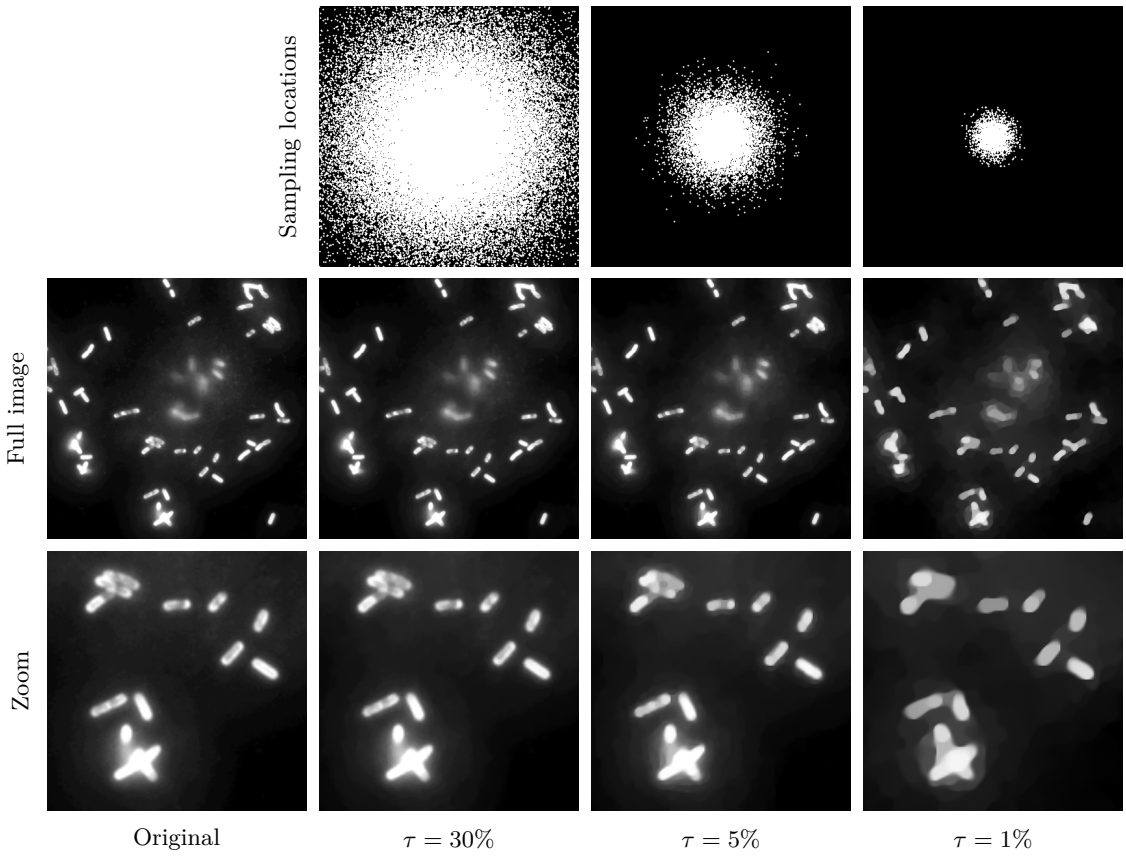

Figure 1. A test image reconstructed from partial measurements in the Fourier space using the TV recovery scheme (7), for different values of the sampling rate $\tau = M/N$ (where N is the number of pixels in the image and M the number of measurements). As τ decreases, the fidelity of the reconstruction to the original image becomes poorer, but the major features (such as the number and the position of the bacterias) can still be extracted even when working with a very low number of measurements.

1.3 Evaluation and description of the reconstructed signals when acquired with few measurements

Although results such as theorem 1.1 are useful to guarantee the theoretical approach used in the CS measurement and reconstruction process, they fail to provide some practical guidelines to those who implement practical CS devices or processes:

- as the hypothesis of these theorems involves knowledge about the original signal (such as the size of its support), they cannot be used to ensure that a particular reconstructed signal is actually identical to the original one;
- as these theorems express some sufficient conditions about the validity of the CS recovery schemes, they are by nature pessimistic: the signal reconstruction can still succeed even if the theorem hypothesis are not fulfilled;
- finally, these results fail to capture the fact that deciding whether the reconstructed signal obtained through a CS recovery scheme is an acceptable estimation of the original signal is not trivial: sometimes, especially when working with fewer measurements than what would be necessary to achieve a perfect recovery, a partial reconstruction of the original signal of sufficient quality – depending on the final application targeted – can still be obtained (see fig. 1).

The goal of this paper is to explore qualitatively how the CS reconstruction quality evolve when the number of measurements varies, and to derive guidelines on how to choose a suitable number of measurements for a particular input image. We will focus on images measured in the Fourier space and reconstructed with a TV recovery scheme (instead of (P_2)):

$$\min \|x\|_{\mathrm{TV}} \quad \text{s.t.} \quad \|Fx - y\| \leq \epsilon \tag{7}$$

This recovery scheme enforces a gradient sparsity prior on the reconstructed image, which is suitable for CS image reconstruction (see Candès, Romberg and Tao[1]).

2. TOWARDS A NUMERICAL EVALUATION OF AN OPTIMAL BOUND FOR THE SAMPLING RATE

2.1 Simulation process

To understand how the sampling rate τ (defined as $\tau = \frac{M}{N}$ where M is the number of measurements and N the number of pixels in the image) affects the performances of the CS recovery scheme, we conducted the following numerical simulations: from a given known original image x_0, we created several sets of randomly sampled Fourier measurements, each of these sets corresponding to a given sampling rate τ. Then, from each of these sets of measurements, we computed the solution $\hat{x}$ of (7), and measured a reconstruction error as follows:

$$\mathrm{RecErr} = \frac{\|\hat{x} - x_0\|_{l_2}}{\|\mu_0 - x_0\|_{l_2}} \tag{8}$$

where μ_0 is equal to the mean value of x_0.

When building a set of measurements, we always sample the central Fourier coefficient (equal to μ_0), which otherwise could not be recovered by the TV minimization scheme. Our sampling patterns also obey a central symmetry invariance, to be coherent with the Hermitian symmetry property exhibited by the Fourier transform of real-valued images. With these settings, thanks to the normalization factor $\|\mu_0 - x_0\|_{l_2}$, we ensure $\mathrm{RecErr}\,(\tau) \to 1$ when $\tau \to 0$.

All simulations were implemented with Matlab, using the freely available NESTA optimization toolbox*, provided by Becker, Bobin and Candès.[14]

2.2 Isotropic shapes

Our first simple experiment consists in reconstructing elementary images composed of a single circular white object on a black background (this would represent for example a single cell visualized in microscopy). The Fourier coefficients were selected with a uniform random scheme: the probability of selecting each coefficient follows an independent Bernoulli law whose parameter is tuned according to the targeted sampling rate. We studied the evolution of the reconstruction error between the CS reconstructed image $\hat{x}$ and the original image x_0 as a function of the sampling rate τ. As the reconstruction error for a given value of the sampling rate depends on the actual location of the samples in the Fourier space, each reconstruction was re-run ten to twenty times with different sampling patterns, and the median error value is reported.

We present some detailed results obtained for a one-disk image with a radius $\rho = 22$ pixels on figure 2 (the image is sized 256×256 pixels). The corresponding curve $\mathrm{RecErr} = f\,(\tau)$ shows three distinct domains:

- for small values of τ, the reconstruction error is constant at a high level: in this domain, the number of Fourier samples is too low to achieve a correct CS reconstruction, and the solution computed from (7) is roughly unstructured;
- for high values of τ, the reconstruction error is also almost constant at a level close to zero: in this domain, the sampling rate is sufficient to perform an exact reconstruction of the original image from the subset of Fourier coefficients that are actually sampled;

*http://www-stat.stanford.edu/~candes/nesta/

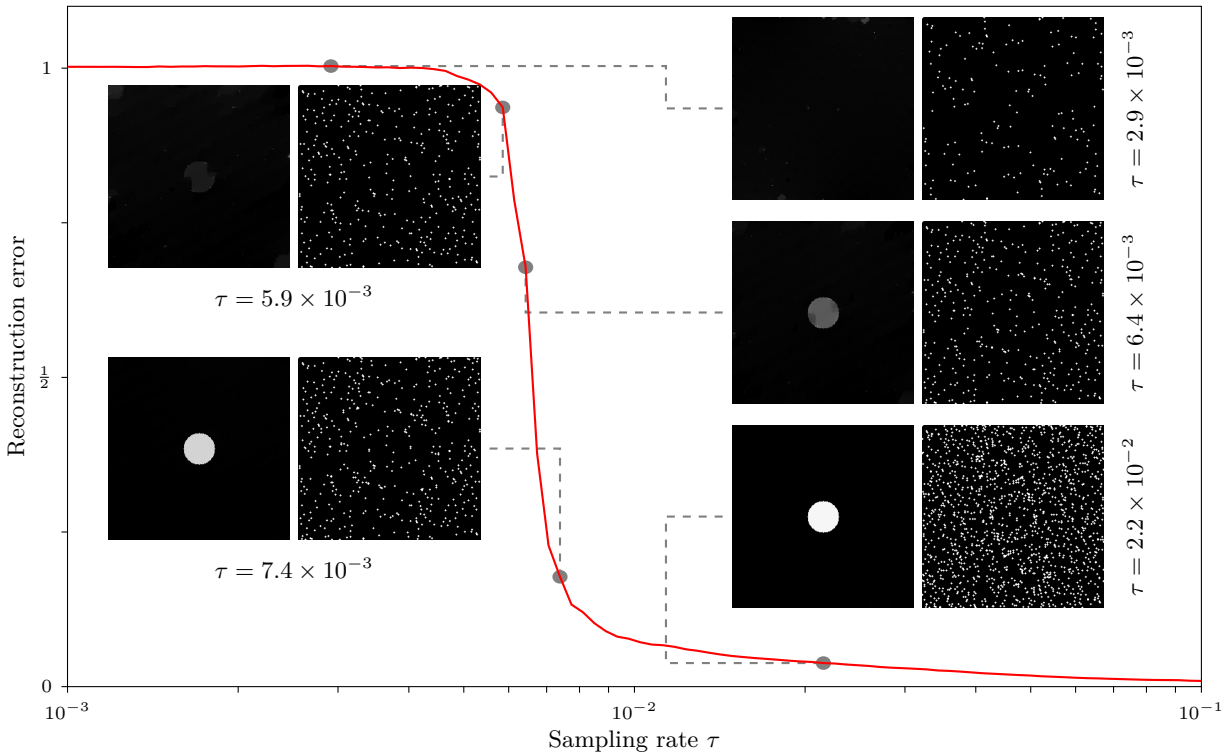

Figure 2. Evolution of the reconstruction error of the same one-disk image with radius $\rho = 22$ pixels for a sampling rate τ in the range $\left[10^{-3}, 10^{-1}\right]$, and five reconstructed images obtained for different values of τ. Each reconstructed image is presented with its associated Fourier sampling pattern. The reconstructed image obtained for $\tau = 2.2 \times 10^{-3}$ is almost identical to the original image.

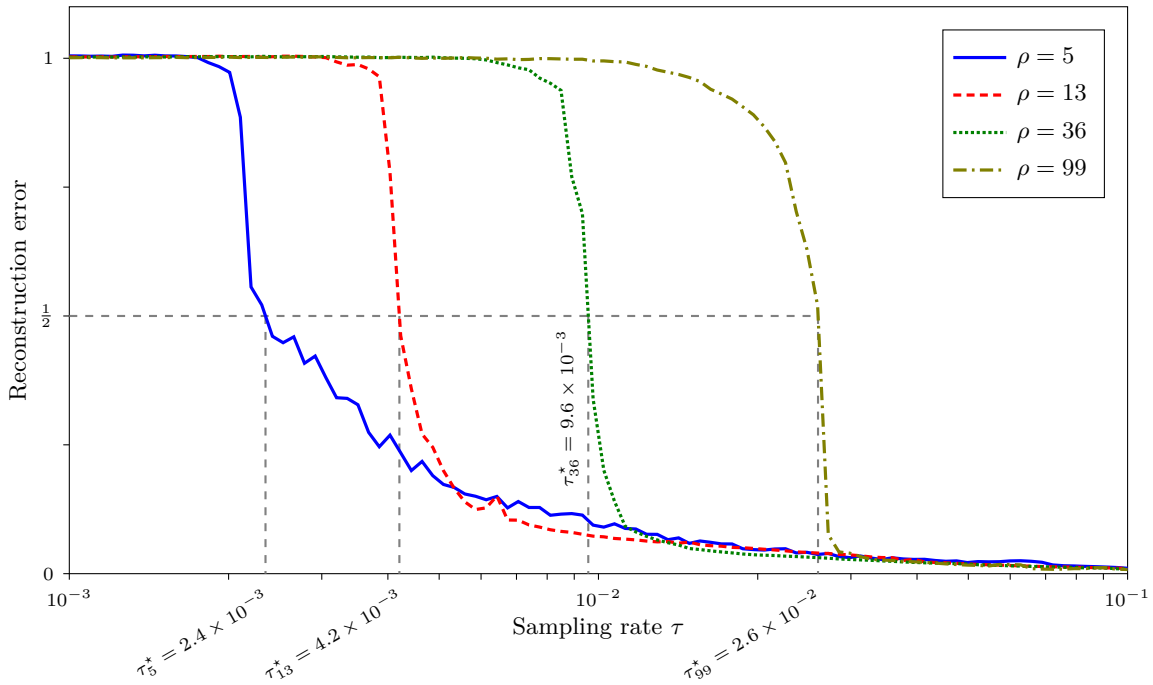

Figure 3. Evolution of the reconstruction error for four one-disk images with various radius ρ, and the associated critical sampling rates $\tau^\star$ extracted from the curves.

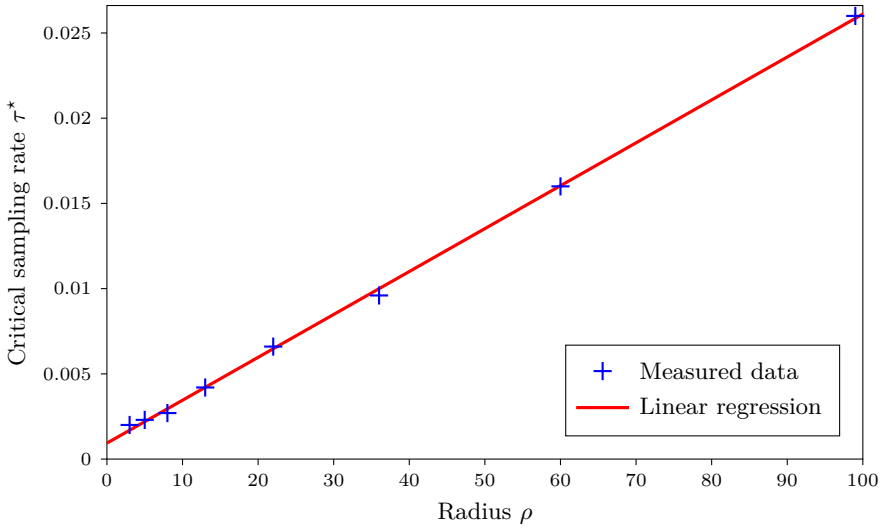

Figure 4. Transition sampling rate $\tau^\star$ for eight values of ρ. A linear regression on these data confirms that, for the single-disk images, $\tau^\star$ obeys a linear increasing law with respect to ρ.

- between these two constant domains, there is a narrow area around a transition sampling rate $\tau^\star$ where the reconstruction error decreases from high value to almost zero.

The value $\tau^\star$ of the sampling rate, as it somehow separates the domain where reconstruction is possible from the domain where it is not, can be interpreted as an empirical measure of the sampling threshold that is defined in a theoretical manner in (3). The fact that this threshold is drastically modified depending on the input image reflects on the variation of the underlying sparsity coefficient S.

There are several possible definitions of the actual value $\tau^\star$ from the curve $\text{RecErr} = f(\tau)$: one could define $\tau^\star$ such that $\text{RecErr}(\tau^\star) = 0.5$ (0.5 being the mean value between the two constant levels of the curve), or decide that $\tau^\star$ is the point where the first derivative of the function takes its maximal absolute value (as the function seems to have an inflexion point in the transition domain); however, as long as the transition domain is sufficiently narrow, all these definitions are likely to be equivalent. For the sake of simplicity, we defined $\tau^\star$ such that $\text{RecErr}(\tau^\star) = 0.5$ in our simulations (see fig. 3); this definition does not depend on the spread of the transition domain.

2.3 Optimal sampling rate and sparsity

When performing a CS reconstruction using the optimization problem (7), we know that the underlying *a priori* hypothesis on the input image is that it has a sparse gradient. In the case of our simple binary images, the number of non-zero gradient coefficients is approximately equal to the perimeter of the object. Then, together with (3), we can make the assumption that the transitional sampling rate $\tau^\star$ is an increasing linear function of the perimeter of the object. Therefore, in the case of our one-disk images, $\tau^\star$ should increase linearly with ρ.

In order to check this hypothesis, we computed the transition sampling rate $\tau^\star$ for eight values of the disk radius ρ. Results in fig. 4 confirm that $\tau^\star$ obeys a linear increasing law with respect to ρ, hence corroborating empirically the theoretical relation (3).

2.4 Optimal sampling rate and shape factor

We also investigated the dependency of the transitional sampling rate $\tau^\star$ with respect to the shape factor of the imaged object. Equation (3) suggests that $\tau^\star$ depends only on S (the number of non-zero gradient coefficients), that is related to the perimeter of the object, but not to its area of the shape factor. Therefore, two objects with the same perimeter should have the same transitional sampling rate, even if one is isotropic (for exemple, a disk) and one has a spatial dimension much larger that the others (for exemple, a flat ellipse).

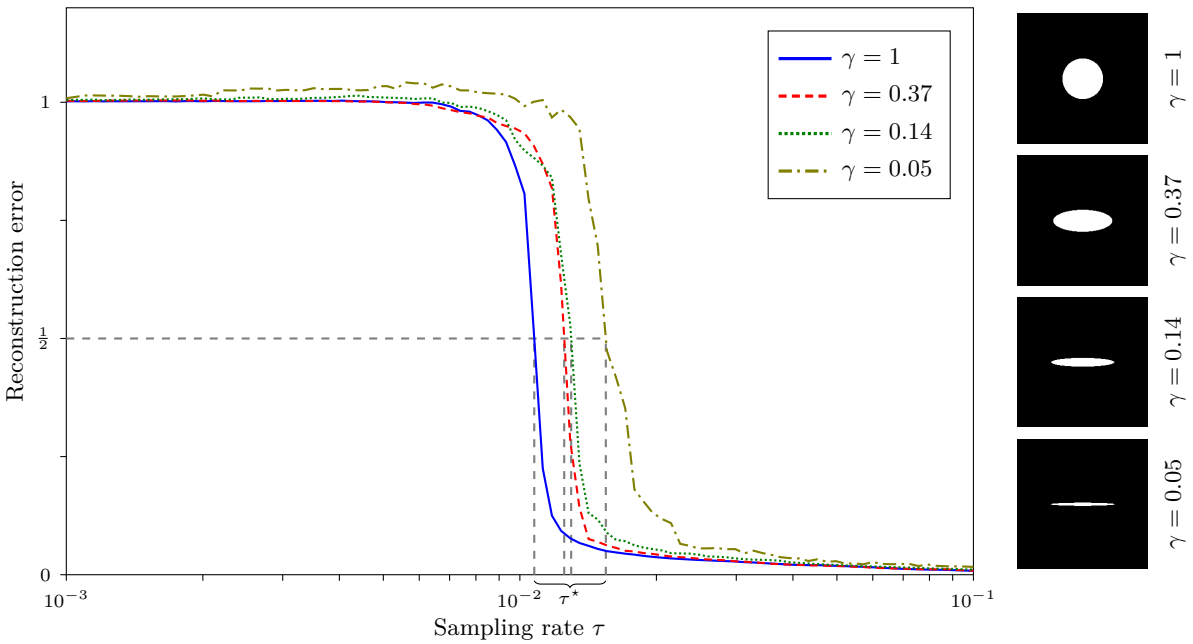

Figure 5. Evolution of the reconstruction error for four ellipses of constant perimeter $p = 250$ pixels but various shape factor γ, and position of the associated critical sampling rates $\tau^\star$. The corresponding test images are presented on the right.

To validate this hypothesis, we followed a similar approach than for the single-disk test images, but we replaced the disks with ellipses of constant perimeter and various eccentricities. By varying the ratio γ between the half minor axis and the half major axis from 1 (circle) to almost 0 (flat shape), we tested shapes with different spatial and frequency characteristics; on the other hand, by setting a constant perimeter, we have maintained a constant TV-based sparsity measure for all the test images: then the observed $\tau^\star$ should be the same for all the inputs. The results are presented on fig. 5.

Although the four curves do not perfectly overlap, the associated transitional sample rates are distributed in a narrow domain, approximately $\left[10^{-2}, 1.7 \times 10^{-2}\right]$. Moreover, this analysis neglects all the effects due to the fact that our test shapes are drawn on a cartesian grid with a non-zero step parameter; in particular, our hypothesis that the number of non-zero gradient coefficients is approximately equal to the perimeter of the object is no longer valid for small disks or very flat ellipses. This explains why the four critical sampling rates are not strictly identical.

2.5 Putting things together

Results presented in sections 2.3 and 2.4 show that the critical sampling rate associated to a binary image composed of one elliptical object is proportional to the perimeter of the object, but does not depend on its shape factor. This is in agreement with the relation (3) stated by Candès and Romberg,[7] which expresses that the minimal number of measurements needed to reconstructed an image through a CS recovery scheme is proportional, for a given number of pixels N, to its sparsity coefficient S. When TV regularization is used to reconstruct binary images, this coefficient S is roughly equal to the length of the boundary between the two binary domains.

Going further, we can study the following question: if the binary image is now composed of several elliptical objects, can we still observe a linear dependency between the critical sampling rate and the size of the boundary between the two binary domains in the image, which is equal to the sum of the perimeters of all the objects? Then, is it possible to predict a suitable sampling rate for CS reconstruction from an *a priori* knowledge of some geometric characteristics of the imaged objects, from which the size of the boundary between the two domains could be computed? An application example where it would make sense to formulate such a knowledge can be

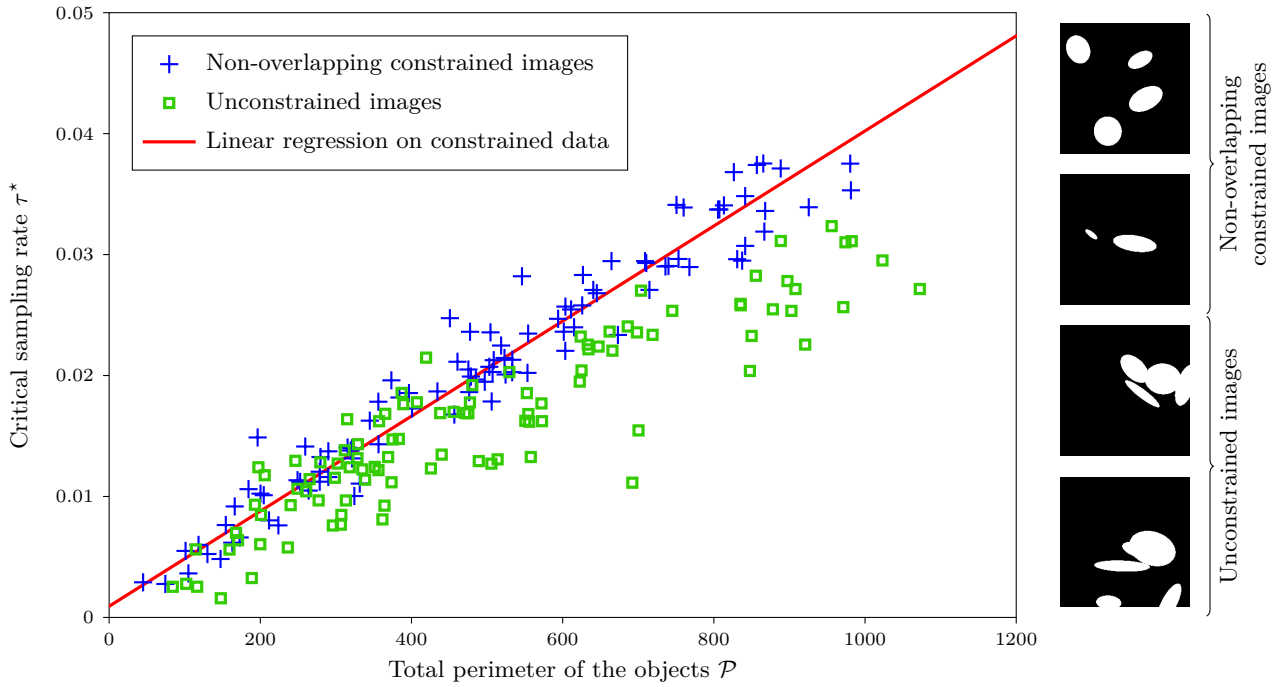

Figure 6. Points $(\mathcal{P}, \tau^\star)$ computed on random binary images composed of ellipses generated with and without enforcing a non-overlapping constraint on them. Examples of such test images are presented on the right.

found in the biological imaging field: if we image a sample containing a fixed number of cells with a non-elastic membrane, a reasonable prediction about the size of the interface between the cells and the medium can be formulated, as this size would not change much over time.

To answer this question, we carried out the following experiment: we generated some test images containing a random number of ellipses, each of them having random perimeter, eccentricity and orientation. Then, for each of these test images, we computed the associated critical sampling rate $\tau^\star$ as well as the total perimeter of the objects $\mathcal{P}$. Results are reported on figure 6.

We carried out two series of experiments:

- First, we prevent ellipses from overlapping and from touching the edges of the image; this constraint ensure that the length of the boundary between the two binary domains of the image is actually equal to the sum $\mathcal{P}$ of the perimeters of the ellipses. The result of a linear regression computed on the points $(\mathcal{P}, \tau^\star)$ collected from these experiments is presented on fig. 6: even if we can observe that some data $(\mathcal{P}, \tau^\star)$ deviate from the predicting model, the general trend of this linear model is relevant. The encountered deviations might be due to the uncertainty in the measure of $\tau^\star$.

- Then, we remove the non-overlapping and non-edge-touching constraint; without it, our simulation conditions become closer to real environment that would be encountered in real-life applications. On the other hand, we no longer ensure that the length of the boundary in the image is equal to $\mathcal{P}$: actually, $\mathcal{P}$ will be greater than the length of the boundary between the two binary domains of the image. Therefore, as observed on fig. 6, the linear predicting model computed with the non-overlapping shapes provides an upper bound on the critical sampling rate for the unconstrained images.

Thus, from a practical point of view, given a prior knowledge on the geometric parameter $\mathcal{P}$, we can predict which sampling rate is suitable for CS reconstruction, although this prediction will be pessimistic if imaged objects overlap.

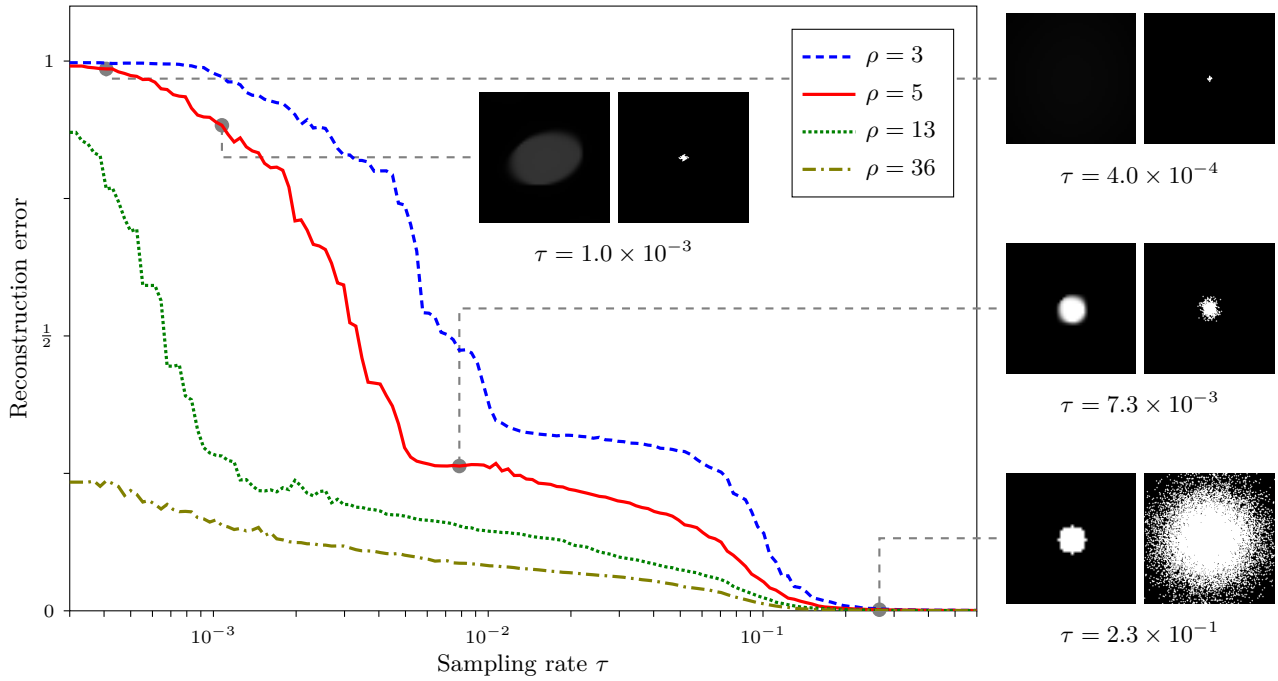

Figure 7. Evolution of the reconstruction error for four one-disk images with various radius ρ, when sampled according to a Gaussian sampling strategy. We present also four zoomed reconstructions of the $\rho = 5$ one-disk test image, with their associated sampling patterns. The reconstructed image obtained for $\tau = 2.3 \times 10^{-1}$ is almost identical to the original image.

3. FURTHER DEVELOPMENTS

3.1 Sampling strategy and filtering effects

The notion of transitional sampling rate is also related to the sampling strategy used to define the position of the measurements in the Fourier space. In all previous simulations, we used a random uniform sampling strategy, which means that the probability of selecting the Fourier coefficient corresponding to the spatial frequency k is given by $p(k) = \tau$, with τ the targeted sampling rate. In this case, no spatial frequency is privileged as $p(k)$ does not actually depend on k. However, alternative sampling strategies exist:

- Candès, Romberg and Tao[1] used a star-shaped sampling pattern when demonstrating the practical recovery capabilities of CS schemes applied to images;
- in a context of 3D MRI imaging, Kim, Narayanan and Nayak[15] used a non-uniform sampling pattern having a small fully sampled area closed to the k-space center;
- with the same modality, Vasanawala *et al.*[16] proposed an original random sampling strategy (called Poisson-disc sampling) which enforces a minimal distance constraint between two consecutive measurements in the k-space;
- Wang and Arce[17] studied several sampling strategies, including the star-shaped sampling pattern, spiral-shaped sampling pattern, and non-uniform random patterns.

These sampling strategies take advantage of the fact that the energy of natural images tends to be concentrated close to the center of the Fourier space. Therefore, allocating more measurements to the low frequencies somehow increases the amount of information collected during the CS measurement process.

To understand the effects of these types of low-frequency biased sampling strategies, we have reproduced the one-disk test image experiments presented in section 2.2; however, instead of allocating measurements in a

random uniform manner, we chose to allocate them according to a Gaussian sampling strategy:

$$p(k) = e^{-\frac{\|k\|_{l_2}^2}{R^2}} \tag{9}$$

where the parameter R is tuned according to the overall targeted sampling rate. This sampling strategy is also the one used to generate the sampling patterns presented in fig. 1. The corresponding curves RecErr $= f(\tau)$ are presented on fig. 7.

Compared to the results presented on fig. 3, the profile of the curves RecErr $= f(\tau)$ is dramatically modified with the Gaussian sampling strategy. Indeed, for the single-disk images with $\rho = 3$ and $\rho = 5$, we can identify at least three domains where the reconstruction error is quite stable, and two transitional domains in between. The two extremal stable domains (which correspond approximately to $\rho < 10^{-3}$ and $\rho > 10^{-1}$) are similar to the stable domains that we observe in the case of random uniform sampling: they correspond respectively to a complete failure of the CS recovery scheme, and to a perfect reconstruction of the original image. On the contrary, the intermediate stable domain observed with the Gaussian random sampling cannot be related to phenomena observed with uniform random sampling; when working with sampling rates in this range, the reconstructed images look very similar to the original one, but have blurred edges: for these reconstructions, the CS recovery procedure works well but induces a low-pass filtering effect on the reconstructed image. This low-pass filtering effect is linked to the Gaussian sampling strategy which allows very few measurements in the high frequency areas of the Fourier space.

Another particularity of the Gaussian sampling strategy is that small objects become harder to retrieve than large ones (meaning that a higher sampling rate is required to reconstruct the small-disk images), which is the inverse trend of what is observed with uniform random sampling. This is well understandable, as the Fourier transform of large objects is concentrated closer to the center of the Fourier space. The fact that CS recovery schemes perform better on input signal that have a larger sparsity coefficient S is however paradoxical.

As a consequence, it appears that defining a notion of critical sampling rate for Gaussian sampling strategy is questionable. The link between such a notion and the sparsity coefficient S of the input signal is probably an interesting question to address in detail.

3.2 Realistic image reconstructions

So far, our simulations were carried out on simple test images with low complexity compared to what is encountered in real ones. Real images have textures, may contain details at various scales, and are often subject to degradation during the acquisition process, resulting in blur and noise. Compared to what is observed on simplistic test images such as those in figures 2, 5 and 6, all these phenomena induce a dramatic increase of the underlying sparsity level S. Actually, most of the real images are not even sparse at all: whatever the reasonable basis used to represent such kind of images, an overwhelming percentage of their coefficients are non-zero. Still, real images have a weakly sparse representation in some adapted basis (such as wavelet basis), which allows the use of CS methods on these kind of signals.

We carried out CS reconstruction simulations on four realistic images, following the protocol described in section 2.1, and using uniform Fourier sampling. The four realistic test images are:

1. the well-known Shepp-Logan phantom image, with strictly piecewise constant regions and sharp edges;
2. the Shepp-Logan image degraded with a small Gaussian blur (using a standard deviation of 1 pixel length for the filter, while the image is 256×256 pixels);
3. a true fluorescence microscopy image of *Shigella* bacteria;
4. a microscopy image of *Lymphocytes T* cells, presenting a high level of noise.

Results of these simulations are presented on fig. 8.

For both Shepp-Logan images, the error curves look very similar to the one obtained for the disks and the ellipses in figures 3 and 5: they present two stable domains where the CS reconstruction process respectively

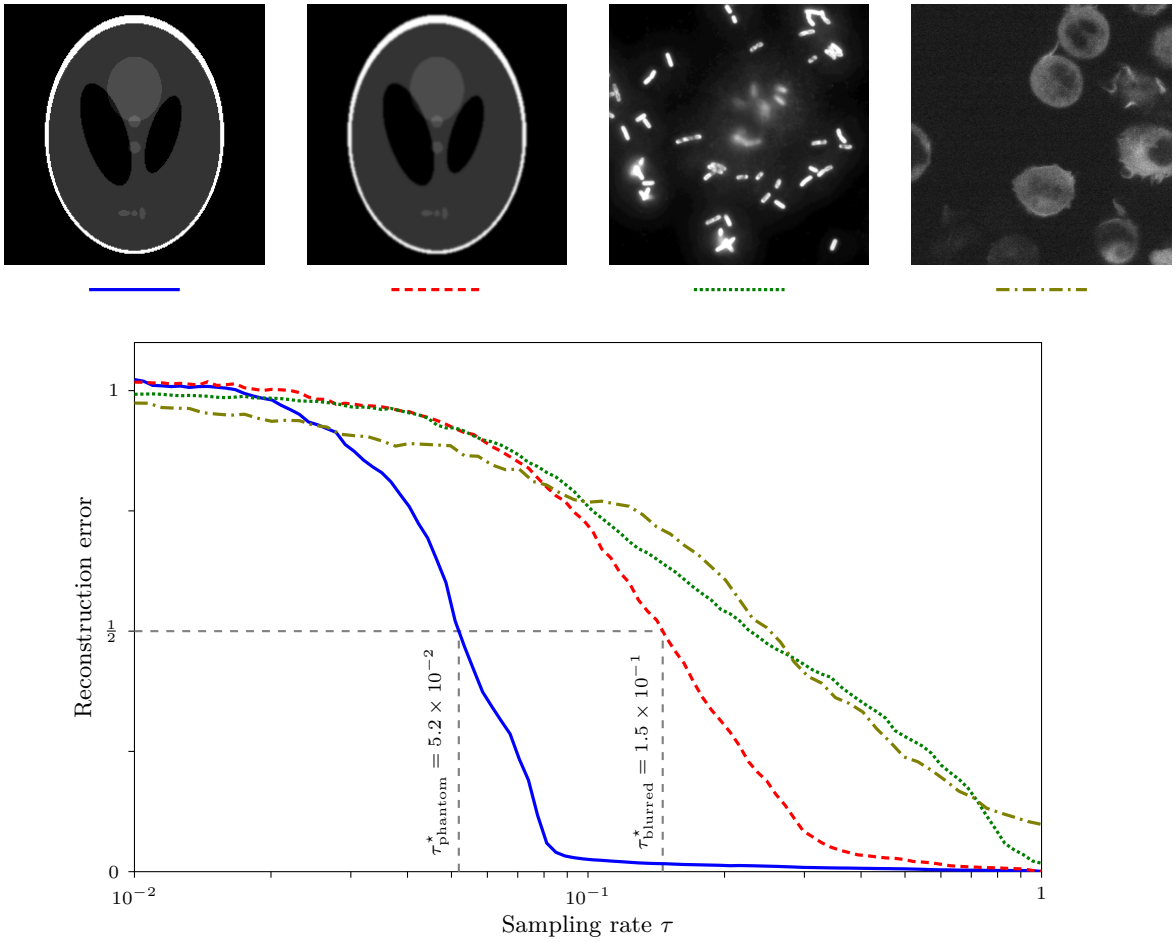

Figure 8. Evolution of the reconstruction error for the four test images presented on the top of the figure, sampled according to a random uniform sampling strategy. These images are, from left to right, the Shepp-Logan test image, a blurred version of Shepp-Logan, and two real biological images, *Shigella* and *Lymphocytes T*.

fails and succeeds, and a narrow transition area between these domains where the relative reconstruction error falls from almost 1 to almost 0 as τ increases. However:

- compared to what was observed with disks and ellipses, the transition between the failure and the success domains occurs at a much higher sampling rate (approximately 10^{-1}, instead of 10^{-2}); moreover, the spread of this transition domain is larger;
- even if the two Shepp-Logan images are very similar (the blurring effect applied on the second image is moderate as it does not lead to any loss of details), both the position and the spread of the transition domain are dramatically changed due to the blur.

Therefore, defining a critical sampling rate for these images still makes sense, even if the accuracy obtained on the corresponding measured values is poorer than for the simple binary images. Together with the theoretical relation (3), this can be explained by the fact that the Shepp-Logan images still have strict underlying sparse structures (in terms of gradient), even if the corresponding sparsity level S becomes much larger as soon as a blurring filter is applied.

On the contrary, in the case of the *Shigella* and *Lymphocytes T* images, the reconstruction error never reaches a stable low level; the reconstruction error associated to the *Lymphocytes T* image does not even reach 0 (even for $\tau = 100\%$ fully sampled reconstructions), because of its high level of noise. As these images are not strictly

sparse, increasing the amount of available information (i.e. the number of measurements) always improves the fidelity of the reconstruction; therefore, defining a critical sampling rate based on reconstruction errors for these images is not as relevant as in the case of binary sparse images.

4. CONCLUSION

In this paper, we proposed an experimental exploration of the conditions allowing perfect CS recovery in a context of image reconstruction through TV minimization and Fourier undersampling. We examined the case of simple binary test images, and exhibited a linear relation between the minimal sampling rate ensuring perfect CS reconstruction and the length of the boundary of the objects. We also discussed the effects induced by a low-frequency favoring sampling strategy (the Gaussian sampling strategy) and the existence of an associated critical sampling rate, and presented some results obtained with realistic images.

REFERENCES

[1] Candès, E., Romberg, J., and Tao, T., "Robust uncertainty principles: exact signal reconstruction from highly incomplete frequency information," *IEEE Transactions on Information Theory* **52**, 489–509 (2006).

[2] Donoho, D. L., "Compressed sensing," *IEEE Transactions on Information Theory* **52**, 1289–1306 (2006).

[3] Donoho, D. L. and Huo, X., "Uncertainty principles and ideal atomic decomposition," *IEEE Transactions on Information Theory* **47**, 2845–2862 (November 2001).

[4] Donoho, D. L. and Elad, M., "Optimally sparse representation in general (non-orthogonal) dictionaries via l_1 minimization," in [*Proceedings of the National Academy of Sciences of the United States of America*], 2197–2202 (2003).

[5] Candès, E. and Tao, T., "Decoding by linear programming," *IEEE Transactions on Information Theory* **51**, 4203–4215 (December 2005).

[6] Candès, E. and Tao, T., "Near-optimal signal recovery from random projections: universal encoding strategies?," *IEEE Transactions on Information Theory* **52**, 5406–5425 (2006).

[7] Candès, E. and Romberg, J., "Sparsity and incoherence in compressive sampling," *Inverse Problems* **23**, 969–985 (2006).

[8] Candès, E., "The restricted isometry property and its implications for compressed sensing," *Compte-rendus de l'Académie des Sciences de Paris* **346**, 589–592 (2008).

[9] Candès, E., Romberg, J., and Tao, T., "Stable signal recovery from incomplete and inacurrate measurements," *Communications on Pure and Applied Mathematics* **59**, 1207–1223 (2006).

[10] Duarte, M. F., Davenport, M. A., Takhar, D., Laska, J. N., Sun, T., Kelly, K. F., and Baraniuk, R. G., "Single-pixel imaging via compressive sampling," *IEEE Signal Processing Magazine* **25**, 83–91 (2008).

[11] Lustig, M., Donoho, D., and Pauly, J. M., "Sparse MRI: the application of compressed sensing for rapid MR imaging," *Magnetic Resonance in Medicine* **58**, 1182–1195 (2007).

[12] Marim, M., Atlan, M., Angelini, E., and Olivo-Marin, J.-C., "Compressed sensing with off-axis frequency-shifting holography," *Optics Letters* **35**, 871–873 (2010).

[13] Le Montagner, Y., Angelini, E., and Olivo-Marin, J.-C., "Comparison of reconstruction algorithms in compressed sensing applied to biological imaging," in [*International Symposium on Biomedical Imaging*], IEEE (2011).

[14] Becker, S., Bobin, J., and Candès, E., "NESTA: A fast and accurate first-order method for sparse recovery," *SIAM Journal on Imaging Sciences* **4**, 1–39 (2011).

[15] Kim, Y.-C., Narayanan, S. S., and Nayak, K. S., "Accelerated three-dimensional upper airway MRI using compressed sensing," *Magnetic Resonance in Medicine* **61**, 1434–1440 (2009).

[16] Vasanawala, S. S., Murphy, M. J., Alley, M. T., Lai, P., Keutzer, K., Pauly, J. M., and Lustig, M., "Practical parallel imaging compressed sensing MRI: Summary of two years of experience in accelerating body MRI of pediatric patients," in [*International Symposium on Biomedical Imaging*], 1039–1043, IEEE (2011).

[17] Wang, Z. and Arce, G. R., "Variable density compressed image sampling," *IEEE Transactions on image processing* **19**, 264–270 (January 2010).